

Master Thesis



Subject

# **Exploring Turing Patterns through the Simulation of Engineered Nodal and Lefty Gene Circuits**

Moritz Schweller

January 8, 2025

Prüfer\*innen: *Prof. Dr. rer. nat. Nicole Radde*  
*Jun. Prof. Dr. Michael Heymann*  
Betreuer: *M.Sc. Amatus Beyer*

Institut für Stochastik und Anwendungen  
Universität Stuttgart  
Prof. Dr. Ingo Steinwart



# Contents

<b>1</b>	<b>Introduction</b>	<b>5</b>
<b>2</b>	<b>Background</b>	<b>7</b>
2.1	Turing Patterns . . . . .	7
2.2	Nodal-Lefty Signaling . . . . .	9
<b>3</b>	<b>Nodal-Lefty Model</b>	<b>13</b>
3.1	Nondimensionalization . . . . .	14
3.2	Nullclines Analysis . . . . .	15
<b>4</b>	<b>Numerical Solution</b>	<b>21</b>
4.1	Spatial Discretization in One Dimension . . . . .	21
4.2	Spatial Discretization in Two Dimensions . . . . .	23
4.3	Temporal Discretization . . . . .	23
4.3.1	Explicit Euler Method . . . . .	24
4.3.2	Heun's Method . . . . .	25
4.3.3	Crank-Nicolson Method . . . . .	26
4.3.4	Strang Splitting Method . . . . .	26
<b>5</b>	<b>Simulation Results</b>	<b>31</b>
<b>6</b>	<b>Modifications to the Nodal-Lefty Model</b>	<b>45</b>
6.1	Derivation of a Modified Model . . . . .	45
6.2	Explicit Receptor Binding . . . . .	48
<b>7</b>	<b>Summary and Outlook</b>	<b>51</b>



# 1 Introduction

The formation of complex spatial patterns from seemingly homogeneous states is a fascinating phenomenon, with applications ranging from the intricate markings on animal coats to the complex formation of organs from a single embryonic cell. Mathematically speaking, these systems are especially interesting, because they contradict the general intuition of diffusion systems converging to a homogeneous steady state. The foundation for the mathematical description of such systems was laid by Alan Turing in his 1952 paper "The Chemical Basis of Morphogenesis" ([10]), which provided a theoretical framework for understanding pattern formation through so-called reaction-diffusion equations. Specifically, Turing demonstrated how a specific interaction of a short-range activator and a long-range inhibitor can lead to stable spatial patterns. In this thesis, we consider a specific example of a gene circuit which is capable of forming Turing patterns: the Nodal-Lefty gene circuit. This circuit was shown to be capable of pattern formation by Sekine et al. [9] in experiments with genetically modified cells. The same study also proposes a mathematical model for the description of the Nodal-Lefty signaling pathway, where pattern formation was observed as well.

This thesis pursues two primary goals: first, to further explore the model proposed by Sekine et al. [9] and its capacity of generating Turing patterns through extensive numerical simulations, and second, to modify the existing mathematical model to more accurately describe observed physical characteristics, specifically allowing for similar diffusion rates for both Nodal and Lefty. Furthermore, the thesis aims to provide a versatile simulation framework for the simulations carried out throughout this thesis, as well as potential modifications or other reaction-diffusion systems.

The thesis is structured as follows: Chapter 2 provides the necessary background for understanding the work presented in later chapters. It begins with a brief overview of Turing patterns, explaining the core concepts of activator-inhibitor dynamics and the role of differential diffusion. The chapter then introduces the Nodal-Lefty signaling pathway and presents the experimental evidence for Turing pattern formation in genetically engineered

cells.

Chapter 3 introduces the mathematical model governing the Nodal-Lefty signaling pathway which was proposed by Sekine et al. [9]. It also carries out a nondimensionalization of the model, simplifying the equations for further analysis and reducing the number of parameters. The chapter ends with the analysis of the equations and its nullclines, providing a theoretical framework for understanding the steady-state behavior.

Chapter 4 details the numerical methods employed to solve the Nodal-Lefty model. It covers various spatial and temporal discretization schemes, discussing each method's advantages and disadvantages regarding stability, accuracy and computational cost. The aim is to clarify the choices made when discretizing the equations in order to allow readers to understand the code and modify it to their needs.

Chapter 5 presents the results of the numerical simulations conducted in this thesis. The chapter explores the parameter space of the Nodal-Lefty model, analyzing the influence of key parameters such as production and diffusion rates on the resulting spatial patterns. The findings are then compared to the theoretical predictions derived from the nullcline analysis.

Chapter 6 addresses the second main goal of this thesis: modifying the Sekine model to account for same diffusion rates for both Nodal and Lefty. It details the derivation of the modified model that incorporates a term for receptor-binding intended to compensate for missing diffusivity difference between Nodal and Lefty.

Finally, the thesis concludes with a summary of the key findings, discussion of their implications and outlook on potential further research questions.

**Code Availability:** All code developed throughout this thesis is publicly available on [GitHub](#) [8]. This includes a flexible simulation framework, designed not only for this specific model but also with the potential for application to other reaction-diffusion systems.



## 2 Background

The development of complex spatial patterns from initially uniform states is a fundamental process underlying many phenomena in biology. The same mechanisms that explain the formation of stripes on a zebrafish (Figure 2.1a) or the complex patterns on a giant pufferfish (Figure 2.1b) can also be used to explain how complex structures like organs are able to form seemingly uniform cells. For that reason, understanding these mechanisms has been a long-standing goal in biology. One important framework that explains these phenomena are Turing patterns. In the first section of this chapter, we introduce the core concepts of Turing patterning. Afterwards, we consider a specific example of a potential Turing mechanism, namely the Nodal-Lefty signaling pathway. Doing so, we provide the necessary context for understanding the mathematical model and subsequent simulation results presented in later chapters.

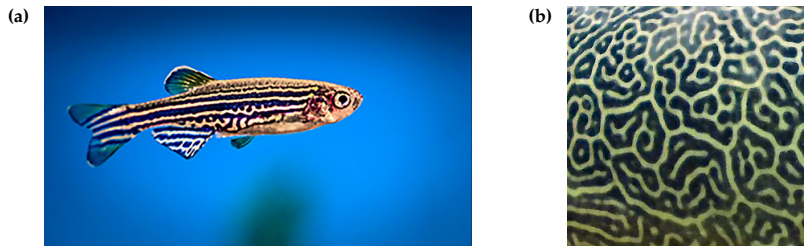


**Figure 2.1:** 2.1a: stripes on a zebrafish [6]. 2.1b: Turing pattern on a giant pufferfish [1].

### 2.1 Turing Patterns

Turing patterns are a concept introduced by Alan Turing in his 1952 paper "The Chemical Basis of Morphogenesis" [10]. Since then, it is viewed as

a fundamental framework that gives an explanation as to how complex patterns in nature, such as stripes and dots, can arise autonomously from seemingly homogeneous states.

Turing considers a model with two chemical species that interact in a so-called reaction-diffusion system. Such a system combines a reaction part, where the species undergo chemical reactions, and a diffusion part that causes the species to spread out in space. The specific reaction considered by Turing is one, where one species ( $A$ ) acts as an activator, promoting the production of the other species ( $B$ ) as well as its own production. At the same time species ( $B$ ) acts as an inhibitor of species ( $A$ ), inhibiting its production. This specific interplay is described as one of two necessary requirements for the formation of Turing patterns.

The second requirement is that the inhibitor ( $B$ ) is of higher diffusivity than the activator ( $A$ ), while degradation rates are similar. A visual explanation for this requirement is given in Figure 2.2.

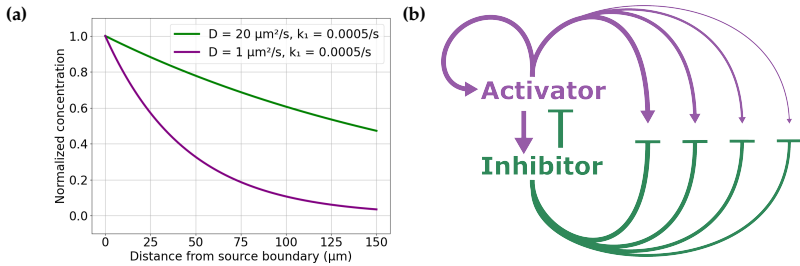


**Figure 2.2:** Visualization of the impact of different diffusion rates on activator-inhibitor systems. In a system with a highly diffusive inhibitor (long-range inhibitor) and a lower diffusive activator (short-range activator), the further one moves from the source, the higher the impact of the inhibitor over the activator. This leads to suppression of further activation in the surrounding areas of the source term, and thus to pattern formation. Graphic adjusted from [5].

Figure 2.2a shows the concentration decline of two species with different diffusion rates as the distance from the source increases. The diffusion rate of one of the species is thereby 20 times higher than the other one, while



the degradation rates are the same. This specific value for the diffusivity ratio coincides with what we will find as the critical value for pattern formation in later chapters. As one moves further from the source, the local inhibitor concentration increases relatively to the activator concentration. Now consider the species of higher diffusivity to be the inhibitor, the lower diffusive one to be the activator. This leads to a scenario as illustrated in Figure 2.2b. Close to the source, the activator promotes both its own production and that of the inhibitor. However, relative concentration of the inhibitor is not high enough to prevent activation. Then, due to the faster diffusion of the inhibitor, it will spread faster to surrounding areas where it suppresses further activation. This is called long-range inhibition. Consequently, activation is limited to local areas in proximity to initial increases in activator concentration, creating what we observe as a pattern.

## 2.2 Nodal-Lefty Signaling

In our case, the two interacting signaling molecules are Nodal and Lefty. The Nodal-Lefty signaling pathway plays a crucial role in early-stage embryonic development. It has been found to be responsible for left-right specification. In other words, it plays a part in determining which side of the embryo is left and right, such that organs like the heart can develop on the correct side. Evidence that the Nodal-Lefty signaling pathway can lead to the formation of Turing patterns is presented by Sekine et al. [9]. In an experiment, HEK293 cells - a commonly used immortalized cell line derived from the kidney of a female fetus - were genetically modified to implement Nodal-Lefty signaling. Nodal signaling was then monitored using a  $(f2)_7$ -luc reporter, which leads to the cells emitting light when the Nodal signaling pathway is active. The results from this setup are shown in Figure 2.3. The experiment initially shows randomly spread small regions of Nodal-Lefty activity or rather  $(f2)_7$ -luc activity. Over time these regions grow in size and intensity. After 36 hours, there is only little growth. From 36 hours to 42 hours only small differences are noticeable: The system has reached its steady state. The heterogeneous distributions of Nodal (and Lefty) is what we call a pattern. The model proposed by Sekine et al. [9] is designed to replicate the behavior that was observed in this experiment. The Nodal-Lefty signaling pathway can be described as shown in Figure 2.4. Extracellular Nodal binds to cell membrane receptors Cryptic and Activin types I and II. The activated receptors indirectly (through the activation of Smads) lead to the activation of the

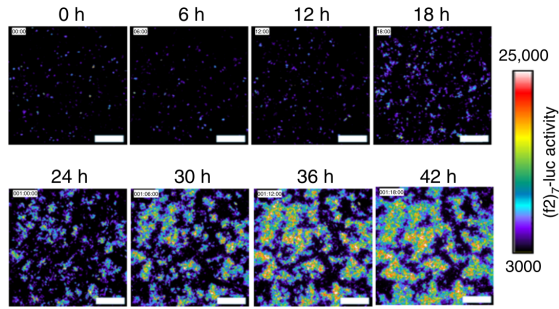


**Figure 2.3:** Time-lapse imaging of HEK293 cells engineered with Nodal-Lefty signaling circuit. Initially, small regions of Nodal activity are spread randomly across the domain. Over time, these regions grow in size and intensity. After 36 hours a mostly stable pattern is observed. (source: Sekine et al. [9])

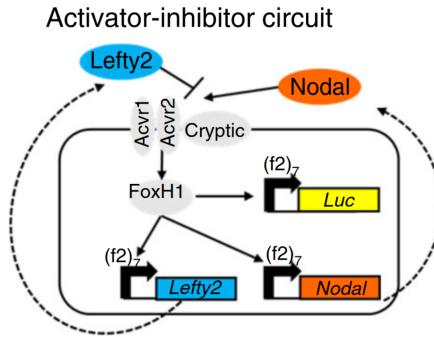


**Figure 2.4:** Activator-inhibitor circuit of Nodal and Lefty. Extracellular Nodal binds to cell membrane receptors, which (through the activation of Smads) lead to the activation of the transcription factor FoxH1. FoxH1 then promotes the transcription of Nodal, Lefty and Luciferase. The latter is responsible for light emission for observation. (source: Sekine et al. [9])

transcription factor FoxH1, which ultimately leads to the transcription of both Nodal and Lefty. Lefty then acts as an inhibitor to Nodal, here through competitive inhibition by binding to the same cell receptors as Nodal. This specific interplay of Nodal and Lefty, together with a lower diffusivity of Nodal compared to Lefty, fulfills the necessary conditions for the formation of Turing patterns.

We have now gained a solid understanding of the necessary conditions for Turing patterns to evolve, as well as the specific functioning of the Nodal-Lefty signaling pathway. Based on that, in the next chapter we will formulate a mathematical model which accurately describes this pathway in order to investigate its capability of forming Turing patterns.



### 3 Nodal-Lefty Model

This chapter lays the foundation for our investigation by introducing the core mathematical model we will be simulating. This system was proposed in Sekine et al. [9] and shown to be able to produce patterns. We will begin by presenting how Nodal-Lefty kinetics can be described as an Activator-Inhibitor circuit (shown in Figure 2.4) and how this circuit transfers to a system of mathematical equations. To facilitate our numerical investigations and simplify our analysis, we will then nondimensionalize these equations, reducing the number of parameters. Finally, we will conduct a preliminary analysis of the model's steady-state behavior using nullcline analysis, revealing the existence of potential stable and unstable states that are crucial for pattern formation. This analysis will set the stage for our computational work, providing a theoretical framework to interpret the results presented in later chapters.

For a mathematical description of the Nodal-Lefty signaling pathway, consider an open domain  $\Omega \subset \mathbb{R}^n$ ,  $n \in 1, 2$  and a time interval  $[0, T]$ . The temporal dynamics of Nodal and Lefty concentrations,  $N(x, t)$  and  $L(x, t)$ , can be described by the following system of reaction-diffusion equations:

$$\frac{\partial N(x, t)}{\partial t} = F(N, L) + D_N \frac{\partial^2 N}{\partial x^2} \quad x \in \Omega, t \in [0, T] \quad (3.1a)$$

$$\frac{\partial L(x, t)}{\partial t} = G(N, L) + D_L \frac{\partial^2 L}{\partial x^2} \quad x \in \Omega, t \in [0, T]. \quad (3.1b)$$

The terms  $F$  and  $G$  denote the reaction parts of the respective equations:

$$F(N, L) = \alpha_N \frac{N^{n_N}}{N^{n_N} + \left[ K_N \left\{ 1 + \left( \frac{L}{K_L} \right)^{n_L} \right\} \right]^{n_N}} - \gamma_N N \quad (3.2a)$$

$$G(N, L) = \alpha_L \frac{N^{n_N}}{N^{n_N} + \left[ K_N \left\{ 1 + \left( \frac{L}{K_L} \right)^{n_L} \right\} \right]^{n_N}} - \gamma_L L. \quad (3.2b)$$

A description of all parameters is given in Table 3.1. Both terms consist of a production term and a degradation term. The production term is modeled by a hill-type equation that includes inhibition by Nodal. It is the same for both  $F$  and  $G$ , since Nodal induces the expression of itself as well as of Lefty (compare Figure 2.4). Only the maximal production rates,  $\alpha_N$  and  $\alpha_L$ , differ.

Parameter	Description	Unit
$\alpha_N$	Maximum production rate of Nodal	$\text{nM min}^{-1}$
$\alpha_L$	Maximum production rate of Lefty	$\text{nM min}^{-1}$
$n_N$	Hill coefficient of activation by Nodal	/
$n_L$	Hill coefficient of inhibition by Lefty	/
$K_N$	Dissociation coefficient of Nodal	$\text{nM}$
$K_L$	Dissociation coefficient of Lefty	$\text{nM}$
$\gamma_N$	Degradation rate of Nodal	$\text{min}^{-1}$
$\gamma_L$	Degradation rate of Lefty	$\text{min}^{-1}$
$D_N$	Diffusion coefficient of Nodal	$\mu\text{m}^2\text{min}^{-1}$
$D_L$	Diffusion coefficient of Lefty	$\mu\text{m}^2\text{min}^{-1}$

**Table 3.1:** List of parameters for Equation (3.1)

### 3.1 Nondimensionalization

We nondimensionalize Equation (3.1) as it reduces the amount of parameters and simplifies the analysis. For this effort, we introduce the dimensionless variables (marked by asterisks):

$$t^* = t\gamma_N, \quad x^* = \frac{x}{\sqrt{D_N/\gamma_N}}, \quad u := \frac{N}{K_N}, \quad v := \frac{L}{K_L} \quad (3.3)$$

The motivation for this definition becomes clear when plugging them into Equation (3.1), as they are designed in way that exactly cancels out the dimensions. We carry out the details for Equation (3.1a) here, as the process is similar for Equation (3.1b). Rearranging (3.3) for  $x$ ,  $t$ ,  $N$  and  $L$ , then plugging them into (3.1a) yields:

$$\frac{\partial(K_N u)}{\partial(\frac{1}{\gamma_N} t^*)} = F(K_N u, K_L v) + D_N \frac{\partial^2(K_N u)}{\partial(\sqrt{\frac{D_N}{\gamma_N}} x^*)^2}.$$

Plugging in (3.2a) and rearranging, we get

$$\begin{aligned} K_N \gamma_N \frac{\partial u}{\partial t^*} &= \alpha_N \frac{K_N^{n_N} u^{n_N}}{K_N^{n_N} u^{n_N} + \left[ K_N \left\{ 1 + \left( \frac{K_L v^{n_L}}{K_L} \right) \right\} \right]^{n_N}} - \gamma_N K_N u + \frac{D_N K_N}{\gamma_N} \frac{\partial^2 u}{\partial x^{*2}} \\ \Leftrightarrow \frac{\partial u}{\partial t^*} &= \underbrace{\frac{\alpha_N}{K_N \gamma_N}}_{=: \bar{\alpha}_N} \frac{u^{n_N}}{u^{n_N} + [1 + v^{n_L}]^{n_N}} - \frac{\gamma_N K_N}{K_N \gamma_N} u + \frac{D_N K_N}{\gamma_N K_N \gamma_N} \frac{\partial^2 u}{\partial x^{*2}} \\ \frac{\partial u}{\partial t^*} &= \bar{\alpha}_N \frac{u^{n_N}}{u^{n_N} + (1 + v^{n_L})^{n_N}} - u + \frac{\partial^2 u}{\partial x^{*2}}. \end{aligned}$$

Following the same process for Equation (3.1b), we get the dimensionless system of equations

$$\frac{\partial u}{\partial t^*} = \underbrace{\bar{\alpha}_N \frac{u^{n_N}}{u^{n_N} + (1 + v^{n_L})^{n_N}}}_{=: f(u, v)} - u + \frac{\partial^2 u}{\partial x^{*2}} \quad (3.4a)$$

$$\frac{\partial v}{\partial t^*} = \underbrace{\bar{\alpha}_L \frac{u^{n_N}}{u^{n_N} + (1 + v^{n_L})^{n_N}}}_{=: g(u, v)} - \bar{\gamma} v + d \frac{\partial^2 v}{\partial x^{*2}} \quad (3.4b)$$

with  $\bar{\alpha}_N = \frac{\alpha_N}{\gamma_N K_N}$ ,  $\bar{\alpha}_L = \frac{\alpha_L}{\gamma_N K_L}$ ,  $\bar{\gamma} = \frac{\gamma_L}{\gamma_N}$  and  $d = \frac{D_L}{D_N}$ . With that, we have effectively reduced the number of parameters from 10 to 6.

For the following sections and chapters we only consider the dimensionless equations, unless stated otherwise. Hence, we drop the asterisks for easier notation.

## 3.2 Nullclines Analysis

A good way of understanding the theoretical behavior of the Nodal-Lefty equations is to analyze the steady states. We are interested in spatially

homogeneous steady states, i.e.  $\partial_t = 0$  and  $\partial_x = 0$ . This leads to a nonlinear system of equations:

$$\begin{aligned} f(u,v) &= 0 \\ g(u,v) &= 0. \end{aligned}$$

Solving these equations would provide the steady-state values of  $u$  and  $v$ . We do so using the *fsolve* function provided by the python library *scipy.optimize*.

To analyze the stability of the steady states, we need to consider the eigenvalues of the Jacobian  $J$  of the reaction terms:

$$J = \begin{bmatrix} \partial_u f(u,v) & \partial_v f(u,v) \\ \partial_u g(u,v) & \partial_v g(u,v) \end{bmatrix}$$

The Jacobian can be calculated numerically using the *sympy* library. Then, we can find the eigenvalues using the *eigvals* function from *numpy.linalg*. Positive eigenvalues indicate an unstable steady state, while negative eigenvalues indicate stable steady states.

In order to illustrate the results, we want to represent the nullclines graphically. Therefore, we rearrange both equations to express  $v$  in terms of  $u$  or vice versa:

$$f(u,v) = 0 \Leftrightarrow v = \left[ (\bar{\alpha}_N u^{n_N-1} - u^{n_N})^{1/n_N} - 1 \right]^{1/n_L} \quad (3.5a)$$

$$g(u,v) = 0 \Leftrightarrow u = \left( \frac{\bar{\gamma}v}{\bar{\alpha}_L - \bar{\gamma}v} \right)^{1/n_N} (1 + v^{n_L}). \quad (3.5b)$$

Figure 3.1 shows the nullclines together with the numerically computed steady states. We observe that the system can have at maximum 3 steady states, two stable and one unstable. In this case, the system can "choose" between the two stable steady states depending on local conditions. The unstable steady state acts as a threshold or boundary between regions dominated by each stable state. This is called bistability, and leads to spatial pattern formation.

The existence and location of the steady states depends on the choice of parameters, specifically the dimensionless production rates,  $\bar{\alpha}_N$  and  $\bar{\alpha}_L$ , the



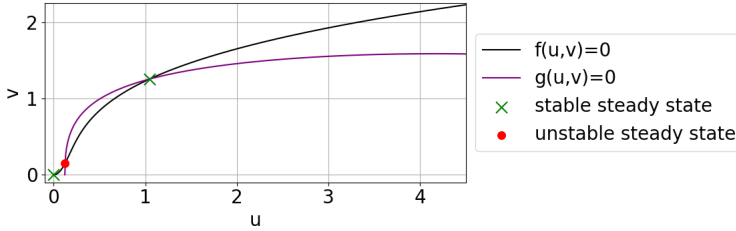


**Figure 3.1:** Visualization of the nullclines and stable/unstable steady states. The functions for the nullclines were calculated analytically. The steady states and their respective stability analysis were computed numerically using *scipy.optimize.fsolve* and *sympy*. Parameters:  $\bar{\alpha}_N = 8.3, \bar{\alpha}_L = 8.3, \bar{\gamma} = 0.83, n_N = 2.0, n_L = 2.5$ .

degradation rate ratio  $\bar{\gamma}$  and the hill coefficients,  $n_N$  and  $n_L$ . However, the steady state at  $(\alpha_N, \alpha_L) = (0,0)$  exists independently of these parameters, which can be easily seen from Equation (3.5). We investigate the dependence of the other two steady states on the maximal productions rates  $\alpha_N$  and  $\alpha_L$ . Figure 3.2b shows the intersections of the nullclines for a fixed  $\alpha_L$  and varying  $\alpha_N$ . We observe that as  $\alpha_N$  decreases, the upper stable state and the unstable steady state approach each other, until they finally merge. If we decrease  $\alpha_N$  beyond that point, only the stable steady state at  $(0,0)$  remains. Figure 3.2c shows the intersections of the nullclines for fixed  $\alpha_N$  and varying  $\alpha_L$ . As  $\alpha_L$  increases, the upper stable steady state and the unstable steady state again approach each other, until only the stable state at  $(0,0)$  remains.

As explained above, bistability requires the existence of all three steady states. When two states merge, a transition from bistability to monostability occurs. In the  $\alpha_N$ - $\alpha_L$  parameter space, these transitions form lines, so-called bifurcation lines.

For simple models, the bifurcation lines can be analytically calculated, by first solving for the steady states and then checking if the derivatives match, as it was done in Gardner et al. [2]. However, the nonlinearity in our reaction terms makes approach impractical. Instead, we opt for a numerical approximation of the bifurcation diagram shown in Gardner et al. [2]. By evaluating a grid of  $(\alpha_N, \alpha_L)$  values, we numerically determine the steady

states, count them, and represent the results in Figure 3.2a. The color coding indicates three distinct regions. The green region of three intersections is the bistable region. The blue region is the upper monostable region, where only the stable steady state at  $(0,0)$  exists. The red region occurs when high  $\alpha_N$  or low  $\alpha_L$  causes the unstable state to merge with the stable state at  $(0,0)$ . Some numerical errors in the calculation of the nullcline intersections occur for lower values of  $\alpha_L$  and  $\alpha_N$ . Except for that, the bifurcation lines are clearly visible, separating the bistable region from the monostable ones.

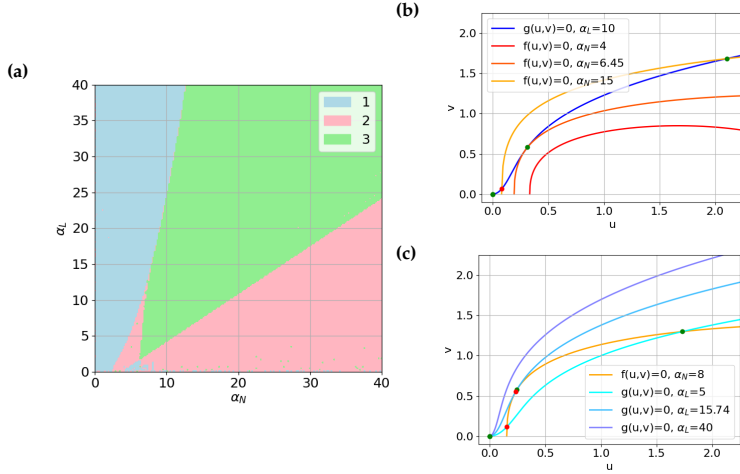


**Figure 3.2:** 3.2a: Numerical approximation of the bifurcation diagram. For each value pair  $(\alpha_N, \alpha_L)$ , the number of intersections of the nullclines was numerically calculated. That number is then shown by color according to the legend. 3.2b: Nullclines  $f(u,v) = 0$  and  $g(u,v) = 0$  for the dimensionless model (3.4). The latter is plotted for  $\alpha_L = 10$  and the former for a range of  $\alpha_N = 4, 6.45, 15$ . Unstable and stable steady states were computed numerically and plotted as red and green dots respectively. 3.2c: Nullclines  $f(u,v) = 0$  and  $g(u,v) = 0$  for the dimensionless model (3.4) for  $\alpha_N = 8$ . and a range of  $\alpha_L = 5, 15.74, 40$ . The remaining parameters were chosen as  $\bar{\gamma}=0.83$ ,  $n_N = 2.0$ ,  $n_L = 2.5$

We have now successfully established the Nodal-Lefty reaction diffusion

model, derived its dimensionless form, and explored the steady-state behavior through nullcline analysis. The latter allowed us to make theoretical predictions for the bifurcation lines in the  $\alpha_N$ - $\alpha_L$  parameter space. The next step is to see if we can confirm these predictions in numerical simulations of the Nodal-Lefty model. In Chapter 4, we will present the spatial and temporal discretization techniques needed to approximate solutions of our model equations, laying the groundwork for the simulation results in Chapter 5.



## 4 Numerical Solution

Having established the Nodal-Lefty model and its dimensionless form in the previous chapter, we now turn our attention to the numerical discretization methods employed for its simulation. A brief description of the discretization method used by Sekine et al. [9] was provided, but the code remained unavailable despite several attempts to contact the author. For that reason, an additional overreaching goal of this thesis is to develop a versatile and robust computational framework, capable of simulating pattern formation in this and potentially other reaction-diffusion systems. To facilitate reproducibility and further development, the entirety of the code developed for this work is also available on a public [GitHub repository](#) [8].

We start with the spatial discretization of the dimensionless equations, first for a 1-dimensional domain in section 4.1, then for a 2-dimensional domain in section 4.2. Following the method of lines, we thereby leave the time variable continuous and do the temporal discretization separately in section 4.3.

### 4.1 Spatial Discretization in One Dimension

For a 1-dimensional domain we have  $\Omega = (0, L)$ . We consider a grid approximation  $\Omega_h$  of  $\Omega$  consisting of grid points  $x_i, i = 1, \dots, N_x$ :

$$\Omega_h = [x_i]_{i=1}^{N_x-1}, \quad x_i = ih_x, \quad h_x = \frac{L}{N_x}.$$

Approximate solutions of (3.4) are grid functions on  $\Omega_h$ , i.e.  $u_i(\cdot) \approx u(x_i, \cdot)$  and  $v_i(\cdot) \approx v(x_i, \cdot)$ . In equation (3.4) we identify a second order spatial derivative in the diffusion term, which we approximate using second order central finite differences:

$$\frac{\partial^2 u}{\partial x^2} = \frac{u_{i+1} - 2u_i + u_{i-1}}{h_x^2} + \mathcal{O}(h_x^2) \quad (4.1a)$$

$$\frac{\partial^2 v}{\partial x^2} = \frac{v_{i+1} - 2v_i + v_{i-1}}{h_x^2} + \mathcal{O}(h_x^2) \quad (4.1b)$$

For the calculation of the second order spatial derivative at position  $x_i$  we need the value at the point itself  $u_i$  as well as its two neighbors  $u_{i-1}$  and  $u_{i+1}$ . This is called a 3-point stencil, as illustrated in Figure 4.1.

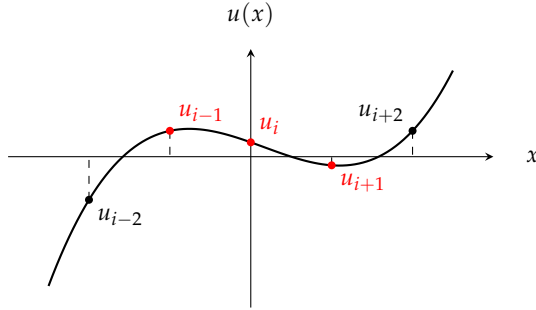


**Figure 4.1:** Visualization of the 3-point stencil of the central difference approximation of the Laplacian in one dimension. The red marked points are used for the approximation of  $\Delta u(x_i) = \partial_x^2 u(x_i)$ .

Plugging this into (3.4) yields the semi-discrete formulation of the dimensionless equations

$$\frac{\partial u_i}{\partial t} = f(u_i, v_i) + \frac{u_{i+1} - 2u_i + u_{i-1}}{h_x^2} \quad (4.2a)$$

$$\frac{\partial v_i}{\partial t} = g(u_i, v_i) + d \frac{v_{i+1} - 2v_i + v_{i-1}}{h_x^2}. \quad (4.2b)$$

Regarding boundary conditions, we choose to employ Zero-Neumann boundary conditions

$$\left. \frac{\partial u}{\partial x} \right|_{\delta\Omega} = 0, \quad \left. \frac{\partial v}{\partial x} \right|_{\delta\Omega} = 0.$$

A simple implementation for this is

$$\begin{aligned} \frac{u_1 - u_0}{h_x} = 0 &\Rightarrow u_0 = u_1, & \frac{u_{N_x} - u_{N_x-1}}{h_x} = 0 &\Rightarrow u_{N_x} = u_{N_x-1} \\ \frac{v_1 - v_0}{h_x} = 0 &\Rightarrow v_0 = v_1, & \frac{v_{N_x} - v_{N_x-1}}{h_x} = 0 &\Rightarrow v_{N_x} = v_{N_x-1}. \end{aligned}$$

With that, equation (4.2) can be solved for a suitable time discretization method.

## 4.2 Spatial Discretization in Two Dimensions

For a 2-dimensional domain  $\Omega = (0, L_x) \times (0, L_y)$  with grid approximation  $\Omega_h \in \mathbb{R}^{N_x \times N_y}$ , defined by

$$\begin{aligned}\Omega_h &= \left\{ (x_i, y_j), i = 1 \dots N_x - 1, j = 1 \dots N_y - 1 \right\} \\ x_i &= ih_x, \quad y_j = jh_y \\ h_x &= \frac{L_x}{N_x}, \quad h_y = \frac{L_y}{N_y},\end{aligned}$$

the second order central difference approximation becomes

$$\begin{aligned}\Delta u(x_i, y_j) &= \frac{u_{i+1,j} - 2u_{i,j} + u_{i-1,j}}{h_x^2} + \frac{u_{i,j+1} - 2u_{i,j} + u_{i,j-1}}{h_y^2} + \mathcal{O}(h_x^2 + h_y^2) \\ \Delta v(x_i, y_j) &= \frac{v_{i+1,j} - 2v_{i,j} + v_{i-1,j}}{h_x^2} + \frac{v_{i,j+1} - 2v_{i,j} + v_{i,j-1}}{h_y^2} + \mathcal{O}(h_x^2 + h_y^2).\end{aligned}$$

This can be seen as a 5-point stencil on a two-dimensional grid, as illustrated in Figure 4.2.

These can be plugged into (3.4) to obtain the semi-discrete formulation. The boundary conditions can be treated in the same way as for the 1-dimensional in both  $x$ - and  $y$ -directions.

## 4.3 Temporal Discretization

For the discretization of the time interval  $\Gamma = [0, T]$ , consider the grid

$$\Gamma_h = \left[ t^k \right]_{k=1}^{N_t-1}, \quad t^k = kh_t, \quad h_t = \frac{T}{N_t}.$$

We denote the numerical approximations by  $u^k \approx u(t^k, \cdot)$  and  $v^k \approx v(t^k, \cdot)$ .

In this section we derive various temporal discretization methods, which each come with their advantages and disadvantages regarding stability, computational cost and ease of implementation.

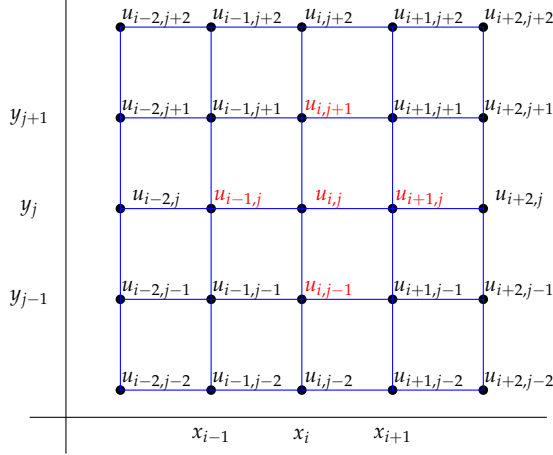


**Figure 4.2:** Visualization of the 5-point stencil of the central difference approximation of the Laplacian. The red marked points are used for the approximation of  $\Delta u(x_i, y_j)$ .

### 4.3.1 Explicit Euler Method

A straightforward approach for the temporal discretization is the Explicit Euler Method. This is also the method used by Sekine et al. [9], therefore we implement it to allow for a better comparison of the results. The idea is to approximate the first order derivative in time by a first order forward finite difference:

$$\frac{\partial u(t^k, \cdot)}{\partial t} = \frac{u^{k+1} - u^k}{h_t} + \mathcal{O}(h_t).$$

The forward finite difference approximates the derivative at  $t = t^{k+1}$  using the values  $u^{k+1}$  and  $u^k$ . Figure 4.3 compares the forward finite difference (used in Explicit Euler) to the backward finite difference (used in Implicit Euler).

Plugging this into the semi-discrete formulations (4.2a) and (4.2b) and rear-



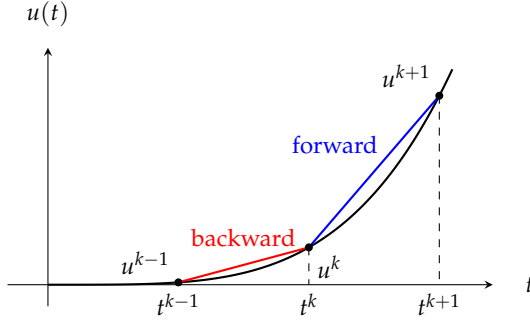


**Figure 4.3:** Visual interpretation of the forward and backward difference quotients at  $t = t^k$ .

ranging for  $u^{k+1}$  yields the update formulas

$$u_i^{k+1} = u_i^k + h_t \left( f(u_i^k, v_i^k) + \frac{u_{i+1} - 2u_i + u_{i-1}}{h_x^2} \right) \quad (4.3)$$

$$v_i^{k+1} = v_i^k + h_t \left( g(u_i^k, v_i^k) + d \frac{v_{i+1} - 2v_i + v_{i-1}}{h_x^2} \right). \quad (4.4)$$

Since this scheme is fully explicit, it comes with the advantage of relatively low computational cost, i.e.  $\mathcal{O}(N_x N_y)$ . However, it is only of convergence order 1, meaning that the error decreases only linearly with respect to the time step. Additionally, it is not unconditionally stable and requires a relatively small time step width  $h_t$ .

### 4.3.2 Heun's Method

Heun's method calculates the next iterate via an intermediate value  $\tilde{y}^{k+1}$ , which is then used to calculate the final approximate solution  $y^{k+1}$ :

$$\begin{aligned} \tilde{U}^{k+1} &= U^k + h_t \text{RHS}(U^k) \\ U^{k+1} &= U^k + \frac{h_t}{2} \left( \text{RHS}(U^k) + \text{RHS}(\tilde{U}^{k+1}) \right) \end{aligned}$$

Here we use the notation  $U = \begin{bmatrix} u \\ v \end{bmatrix}$  and  $\text{RHS}(U) := \begin{bmatrix} f(u,v) + \Delta u \\ g(u,v) + d\Delta v \end{bmatrix}$ .

It can be shown that Heun's method is of order 2. However, the stability of the method remains conditional, as it is still an explicit method.

### 4.3.3 Crank-Nicolson Method

An implicit, second order method is the Crank-Nicolson method. The update formula is the following:

$$U^{k+1} = U^k + \frac{h_t}{2} \left( \text{RHS}(U^k) + \text{RHS}(U^{k+1}) \right). \quad (4.5)$$

### 4.3.4 Strang Splitting Method

In order to avoid the time step limitation of explicit methods, we can choose an implicit method, which usually comes with unconditional stability. However, this brings up another issue: The system of equations (3.4) includes a nonlinear reaction term. Employing an implicit discretization method would mean having to solve a nonlinear system of equations in each time step, which is highly expensive. So-called operator splitting schemes present a solution to this problem. One popular operator splitting scheme is the *Strang splitting* scheme, which we will choose here.

The idea is to split (3.4) into its reaction and diffusion part and treat them as separate PDEs:

$$\frac{\partial}{\partial t} U = \frac{\partial}{\partial t} \begin{bmatrix} u \\ v \end{bmatrix} = \begin{bmatrix} f(u,v) \\ g(u,v) \end{bmatrix} =: \mathcal{L}_1(u,v) = \mathcal{L}_1(U) \quad (4.6a)$$

$$\frac{\partial}{\partial t} U = \frac{\partial}{\partial t} \begin{bmatrix} u \\ v \end{bmatrix} = \frac{\partial^2}{\partial x^2} \begin{bmatrix} u \\ dv \end{bmatrix} =: \mathcal{L}_2(u,v) = \mathcal{L}_2(U). \quad (4.6b)$$

Here, we use the notation  $U := \begin{bmatrix} u \\ v \end{bmatrix}$ .

Equation (4.6a) includes the nonlinear reaction kinetics, and should thus be treated explicitly. Equation (4.6b) is now a pure diffusion equation. Diffusion equations are generally considered stiff and thus should be treated implicitly.

The Strang splitting method involves three substeps. First we take half a time step with the  $\mathcal{L}_1$  operator, then a full step with the  $\mathcal{L}_2$  operator, and

finally another half step with the  $\mathcal{L}_1$  operator. In each substep, the solution from the previous substep is taken as a starting point. During a time interval  $[t^k, t^{k+1}]$ , the algorithm can be written as:

$$\frac{dU^*}{dt} = \mathcal{L}_1(U^*), \quad U^*(t^k) = U(t^k), \quad t \in [t^k, t^k + \frac{h_t}{2}], \quad (4.7a)$$

$$\frac{dU^{**}}{dt} = \mathcal{L}_2(U^{**}), \quad U^{**}(t^k) = U^*(t^k + \frac{h_t}{2}), \quad t \in [t^k, t^{k+1}], \quad (4.7b)$$

$$\frac{dU^{***}}{dt} = \mathcal{L}_1(U^{***}), \quad U^{***}(t^k + \frac{h_t}{2}) = U^{**}(t^{k+1}), \quad t \in [t^k + \frac{h_t}{2}, t^{k+1}]. \quad (4.7c)$$

The procedure is illustrated in Figure 4.4.

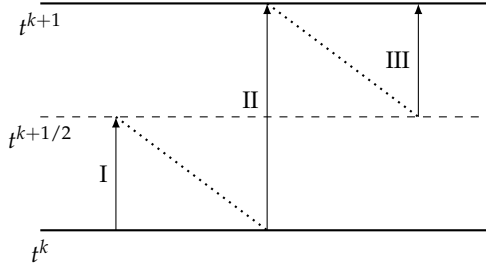


**Figure 4.4:** Three-step algorithm of the Strang-splitting scheme (adjusted from [7])

It can be shown that this procedure allows for a second order accurate scheme.

### Explicit Euler + Implicit Euler

The most straightforward choice of time stepping schemes is the Explicit Euler method for steps (4.7a) and (4.7c), and the Implicit Euler method for

step (4.7b). The algorithm (4.7) becomes

$$U^* = U^k + \frac{h_t}{2} \mathcal{L}_1(U^k) \quad (4.8a)$$

$$U^{**} = U^* + h_t \mathcal{L}_2(U^{**}) \quad (4.8b)$$

$$U^{k+1} = U^{**} + \frac{h_t}{2} \mathcal{L}_1(U^{**}). \quad (4.8c)$$

The Implicit Euler step (4.8b) involves the solution of a linear system of equations. Plugging in the 1D spatial discretization by central differences (4.1) we get

$$U_i^{**} = U_i^* + h_t \left( \frac{U_{i+1}^{**} - 2U_i^{**} + U_{i-1}^{**}}{h_x^2} \right), \quad i = 1, \dots, N_x - 1,$$

which can be written as

$$\left( \mathbf{I} - \frac{h_t}{h_x^2} \mathbf{A} \right) \cdot \mathbf{U}^{**} = \mathbf{U}^* \quad (4.9)$$

with

$$\mathbf{A} = \frac{1}{h_x^2} \begin{bmatrix} -2 & 1 & 0 & \cdots & 0 \\ 1 & -2 & 1 & \cdots & 0 \\ 0 & 1 & -2 & \cdots & 0 \\ \vdots & \vdots & \vdots & \ddots & \vdots \\ 0 & 0 & 0 & 1 & -2 \end{bmatrix}, \quad \mathbf{U}^* = \begin{bmatrix} U_1^* \\ \vdots \\ U_i^* \\ \vdots \\ U_{N_x-1}^* \end{bmatrix}, \quad \mathbf{U}^{**} = \begin{bmatrix} U_1^{**} \\ \vdots \\ U_i^{**} \\ \vdots \\ U_{N_x-1}^{**} \end{bmatrix}.$$

The linear system of equations (4.9) can be solved using methods from numerical linear algebra. In our code, we use the *spsolve* function from the *scipy.sparse.linalg* library.

### Heun + Crank-Nicolson

Using first order schemes such as Explicit and Implicit Euler does not make use of the potential 2nd order nature of the Strang splitting method. A second order temporal discretization would be advantageous, as we already have a second order spatial discretization. Suitable second order schemes

are the explicit Heun scheme and the implicit Crank-Nicolson scheme. The Strang splitting algorithm (4.7) becomes

$$U^* = U^n + \frac{h_t}{4} (\mathcal{L}_1(U^n) + \mathcal{L}_1(\tilde{U})), \tilde{U} = U^n + \frac{h_t}{2} \mathcal{L}_1(U^n) \quad (4.10a)$$

$$U^{**} = U^* + \frac{h_t}{2} (\mathcal{L}_2(U^*) + \mathcal{L}_2(U^{**})) \quad (4.10b)$$

$$U^{n+1} = U^{**} + \frac{h_t}{4} (\mathcal{L}_1(U^{**}) + \mathcal{L}_1(\tilde{U})), \tilde{U} = U^{**} + \frac{h_t}{2} \mathcal{L}_1(U^{**}). \quad (4.10c)$$

Inserting the 1D spatial discretization (4.1) into (4.10b) we get

$$U_i^{**} = U_i^* + \frac{h_t}{2} \left( \frac{U_{i+1}^* - 2U_i^* + U_{i-1}^*}{h_x^2} + \frac{U_{i+1}^{**} - 2U_i^{**} + U_{i-1}^{**}}{h_x^2} \right), \quad i = 1, \dots, N_x - 1,$$

which can be rewritten as

$$\left( \mathbf{I} - \frac{h_t}{h_x^2} \mathbf{A} \right) \cdot \mathbf{U}^{**} = \left( \mathbf{I} + \frac{h_t}{h_x^2} \mathbf{A} \right) \mathbf{U}^* \quad (4.11)$$

with the previous definitions of the matrices  $\mathbf{A}$ ,  $\mathbf{U}^{**}$  and  $\mathbf{U}^*$ . This linear system of equations can again be solved using methods from numerical linear algebra.

With that, we have found a discretization method that is stable and of order 2 in space and time.



## 5 Simulation Results

This chapter presents the results of our computational investigation of the Nodal-Lefty model. Our initial simulations with the parameters provided by Sekine et al. [9] did not reproduce the expected patterns, neither for the original equations (3.1) nor for the dimensionless equations (3.4). Therefore, we first introduce modifications to the original parameter set which allow us to observe pattern formation.

Next, we analyze a representative simulation result to illustrate the general behavior of the Nodal-Lefty model. We then investigate the model's behavior when varying the maximal production rates of Nodal and Lefty,  $\alpha_N$  and  $\alpha_L$ . To do so, we construct a phase diagram over the  $\alpha_N$ - $\alpha_L$  parameter space and compare the observations to the theoretical behavior according to the bifurcation diagram derived in chapter 3. Furthermore, we explain how with various choices of  $\alpha_N$  and  $\alpha_L$  we are able to generate diverse spatial patterns. Finally, we analyze the influence of the diffusion rates,  $D_N$  and  $D_L$ , on the formation of patterns and compare it to results we were able to find in the literature.

The choice of parameters turned out to be crucial in determining whether patterns could be observed. Table 5.1 presents the three parameter sets used in this study. The original parameter set *Original* is taken from Sekine et al. [9] and was modified to obtain the set *Adjusted* by switching  $K_N$  with  $K_L$ . The set *New* differs from *Original* in almost every parameter, and was found by trial and error.

We were not able to observe pattern formation using the parameter set *Original*. This could have various reasons, such as different choices for the temporal and spatial step widths or other details of the discretization method and its implementation, as these were not specified. The initial conditions were also not specified, although a model capable of pattern formation should be able to do so for a variety of initial conditions. Our implementation of the model was able to generate spatial patterns using the sets *Adjusted* and *New*. For the first section of this chapter, we look at the

Original	Adjusted	New
$n_N = 2.63$	$n_N = 2.63$	$n_N = 2.0$
$n_L = 1.09$	$n_L = 1.09$	$n_L = 2.5$
$K_N = 9.28$	$K_N = 14.96$	$K_L = 1.0$
$K_L = 14.96$	$K_L = 9.28$	$K_N = 1.0$
$\gamma_N = 2.37e - 3$	$\gamma_N = 2.37e - 3$	$\gamma_N = 1.2$
$\gamma_L = 5.65e - 3$	$\gamma_L = 5.65e - 3$	$\gamma_L = 1.0$
$D_N = 1.96$	$D_N = 1.96$	$D_N = 1.96$
$D_L = 56.39$	$D_L = 56.39$	$D_L = 56.39$

**Table 5.1:** Pattern formation was observed in 2 modifications of the *original* parameter set provided by Sekine et al. [9], denoted by *Adjusted* and *New*. The parameter set *Adjusted* retains all parameters from the original set except for a switch of  $K_N$  with  $K_L$ . The parameter set *New* modifies almost all original parameters except the diffusion rates.

results produced when using *New*, and then turn to the *Adjusted* set later.

In order to illustrate the general behavior of the Nodal-Lefty model, we consider a representative result of a 2-dimensional simulation of the dimensionless equations. Figure 5.1a shows the emergence of a complex pattern from a random initialization in both Nodal and Lefty. Nodal exhibits a heterogeneous distribution with distinct regions of high and low expression, with the high state revolving around  $u = 2.1$  and the low state at  $u = 0$ . Lefty, on the other hand, displays a more uniform distribution with less pronounced variations. This difference can be attributed to Lefty's higher diffusion rate, which tends to smooth out spatial variations.

The areas of high and low expression in Nodal and Lefty overlap. This is consistent with the literature for reaction-diffusion systems of this type. As Murray explains in his book "Mathematical Biology II: Spatial Models and Biomedical Applications" ([4], p.88), a reaction-diffusion system with a self-activating activator  $u$  and an inhibitor  $v$ , which inhibits not only  $u$ , but also itself, the resulting patterns will be of high and low density in the same regions. Additionally, the pattern observed in Figure 5.1a seems to be stable also for longer simulation times, a key characteristic of Turing patterns.

Similar observations can be made for the 1-dimensional simulation in Fig-



---

ure 5.1b, using the same parameters as for the 2-dimensional simulation from Figure 5.1a. With only one spatial dimension available, the pattern is expressed as a periodic wave over the domain. As with the 2-dimensional simulation, the Nodal distribution exhibits larger amplitudes, while Lefty is more muted. The maximum and minimum values of the amplitudes match the ones observed in 5.1a. The only significant difference to the 2d-simulation is that the extra dimension allows for more complex pattern formations with no apparent periodicity, whereas in one dimension the pattern is simply a periodic wave.

An important advantage of the 1d-simulation is the significantly lower computational cost, which is especially beneficial in later experiments where multiple and longer simulations are necessary.

Next, we investigate the influence of the maximal production rates of Nodal and Lefty,  $\alpha_N$  and  $\alpha_L$ , on pattern formation. Figure 5.2a depicts a phase diagram over the  $\alpha_N$ - $\alpha_L$  parameter space. For  $40 \times 40$  combinations of  $\alpha_N$  and  $\alpha_L$ , each pair is mapped to the difference of the global maximum and minimum Nodal concentration at the end of a 1-dimensional simulation. The difference is represented by color intensity according to a colormap.

The region of pattern formation, the bistable region, is clearly distinguishable from the areas where no patterns are formed. As the production rates increase, the size of the bistable region increases. This is consistent with the findings of Gardner et al. [2] for a toggle switch model.

The theoretical bifurcation lines from the previous nullclines analysis, depicted once again in Figure 5.2b, were already using the parameter set *New*. We can therefore compare the bistable and monostable regions to the ones actually observed in our simulations, presented in Figure 5.2a. We observe that they mostly overlap with the theoretically predicted regions. The fact that the match is not perfect, could have various reasons. First of all, it is important to remember that the criterion we used to produce Figure 5.2a was simply the difference between the maximal and minimal Nodal concentration at the end of the simulation. Therefore, we do not know if the pattern was stable or not. Running simulations for some instances close to the practically observed boundary of the bistable region does in fact produce patterns that are not stable for reasonably long simulation times.

Additionally, Figure 5.2b is also only a numerical approximation of the bifurcation diagram. The exact bifurcation lines might deviate slightly. Either way, we can not expect the numerical simulations to match the theoretical predictions exactly. Especially in close proximity to the bifurcation

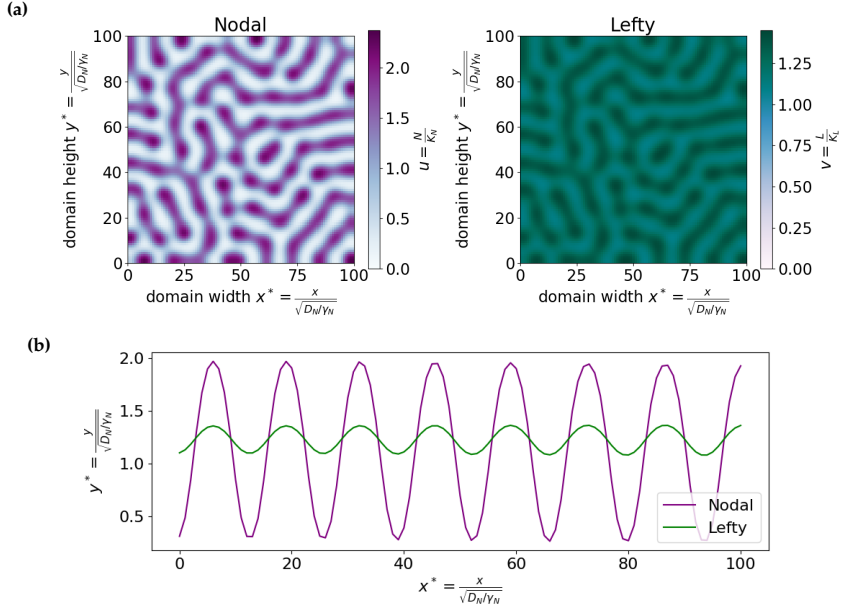


**Figure 5.1:** Simulation of the dimensionless Nodal-Lefty model using the parameter set *New* (see Table 5.1) and random initialization (uniformly distributed using `numpy.random.rand` with seed 0) for a simulation time of  $t^* = 100$ . Furthermore, the max. production rates are chosen as  $\alpha_N = 9.0$  and  $\alpha_L = 8.0$ . **5.1a:** Two-dimensional simulation. **5.1b:** One-dimensional simulation.

lines, small numerical inaccuracies will have a greater influence on the final outcome.

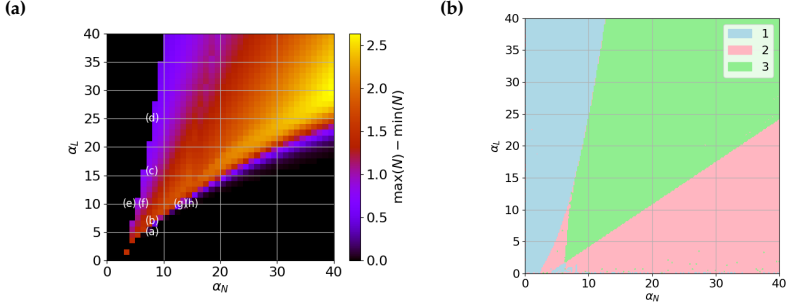


**Figure 5.2:** Using the parameter set *New*, patterns are formed when choosing the max. production rates  $\alpha_N$  and  $\alpha_L$  in the correct ranges. **5.2a:** Phase diagram of max. production rates of Nodal and Lefty  $\alpha_N$  and  $\alpha_L$ . For each combination of production rates, the difference between the global maximum and minimum Nodal concentration of 1d simulations at  $t^* = 100$  is shown by color. **5.2b:** Numerical approximation of the bifurcation diagram for the parameter set *New*, as derived in chapter 3.

We further explore the differences in pattern formation within the bistable region observed in Figure 5.2a. Therefore, we run 2-dimensional simulations for 8 pairs of  $(\alpha_N, \alpha_L)$ , which are presented in Figure 5.3. The Figures 5.3a - 5.3h correspond to the labels (a) - (h) in Figure 5.2a.

A first observation is that the two stable areas in Figure 5.2a of no pattern formation do both yield homogeneous distributions, however their values differ. In the upper stable region every point in space reaches the upper state at  $u \approx 2$ . In the lower stable region all points converge to the lower state  $u = 0$ . These values are in line with the theoretical ones according to the nullclines.

Furthermore, we observe that choices of  $(\alpha_N, \alpha_L)$  inside the bistable region, but closer to the upper boundary, show smaller discrete areas of higher Nodal concentration with large spaces of zero concentration between them. Choices closer to the lower boundary of the bistable region show highly interconnected patterns with only small regions of zero concentration.

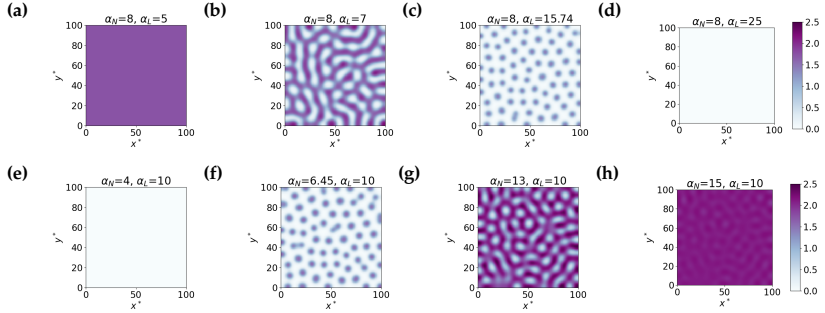


**Figure 5.3:** Pattern formations in Nodal concentration in 2-dimensional simulations for selected combinations of  $\alpha_N$  and  $\alpha_L$  at  $t^* = 100$ . The labels 5.3a - 5.3h correspond to the ones depicted in Figure 5.2a.

Lastly, we investigate the influence of the diffusion rates on pattern formation. Since, we are working with the dimensionless equations, only the ratio  $d = \frac{D_L}{D_N}$  is important. Figure 5.4a shows the difference between the global maximum and minimum Nodal concentrations as a function of the diffusion ratio  $d$ . The difference was measured in 1-dimensional simulations.

The plot reveals a critical diffusion ratio around  $d = 20$ , below which pattern formation is suppressed. Above this threshold, the system exhibits pattern formation. The more  $d$  increases over 20, the larger the difference between the high and low state becomes. Ultimately, the difference seems to converge to an upper limit.

Figures 5.4b - 5.4e depict the Nodal distribution at  $t^* = 500$  in 2-dimensional simulations for  $d = 18, 20, 22, 100$ . Figure 5.4b confirms that for  $d < 20$  no pattern is formed. Figure 5.4c shows the result exactly at the threshold  $d = 20$ . Here we observe a highly interconnected pattern with small low state regions. Figure 5.4d is slightly above the threshold with  $d = 22$ . However, the high state regions are already less interconnected, and we observe longer lines of low state regions. Figure 5.4e shows the result for a relatively high ratio  $d = 100$ . Here, high state regions are not connected and only appear as dots. However, the pattern is much more pronounced with a much larger concentration difference between the two regions.

Other models from literature, such as in Müller et al. [5], found the threshold

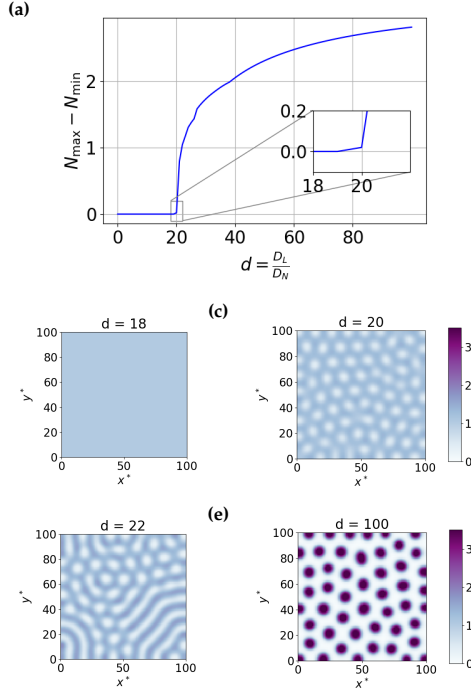


**Figure 5.4:** Dependence of pattern formation on diffusion rate ratio  $d = \frac{D_L}{D_N}$  using the parameter set *New*. **5.4b - 5.4e:** Pattern in Nodal concentration at  $t^* = 500$  for 2-dimensional simulations for 4 exemplary diffusion ratios  $d = 18, 20, 22, 100$ .

value of the clearance-normalized diffusivity ratio between  $\mathcal{R} = (\frac{D_L}{\gamma_L})/(\frac{D_N}{\gamma_N}) = 5 - 15$ . Our value computes as  $\mathcal{R} \approx 8.3$ , confirming the findings of these prior studies.

Having explored the behavior of the model with the modified parameter set *New*, we now turn our attention to the results obtained using *Adjusted*, which is more closely related to the original parameter set from Sekine et al. [9], as it only switches  $K_N$  with  $K_L$ . Figure 5.5a shows the phase diagram over the  $\alpha_N$ - $\alpha_L$  parameter space, analogously to Figure 5.2a. We also calculate the bifurcation diagram resulting from the nullclines again for the *Adjusted* parameters, shown in Figure 5.5b. Qualitatively, the phase diagram of *Adjusted* exhibits similar features to that of *New*. A distinct bistable region of pattern formation is observed, however the specific boundaries of the bistable region and the range of Nodal expression levels differ between the two parameter sets. Especially the upper monostable region is much smaller compared to the one from Figure 5.2a, which is confirmed by the bifurcation diagram in Figure 5.5b. These changes are to be expected, as most of the parameters were changed.

Since the parameter set *Adjusted* is closely related to the original parameter set, Figure 5.6a was produced to serve as a comparison to Figure 5.6b, which was produced by Sekine et al. [9].

The bistable region roughly matches, although not exactly. This could be partly due to the different criteria used to detect pattern formation, and of course due to the switch of  $K_N$  and  $K_L$ .

Figures 5.7a and 5.7b depict the nullclines of the system using the parameter set *Adjusted*. A notable difference is that in contrast to the nullclines of *New*, now the unstable steady state (marked by a red cross) is generally much closer to the stable steady state at  $(u,v) = (0,0)$ . This could explain why the bistable regions in Figure 5.5a and Figure 5.5b differ more than with the previous parameter set *New* (compare to Figure 5.2a and 5.2b respectively). When the two steady states are in very close proximity to each other, it makes the numerical calculation of the steady states more prone to errors, as well as the numerical simulation of the system less stable.

Figure 5.8 presents a series of 2D simulations of the Nodal-Lefty model, illustrating the types of patterns that emerge when choosing  $(\alpha_N, \alpha_L)$  from

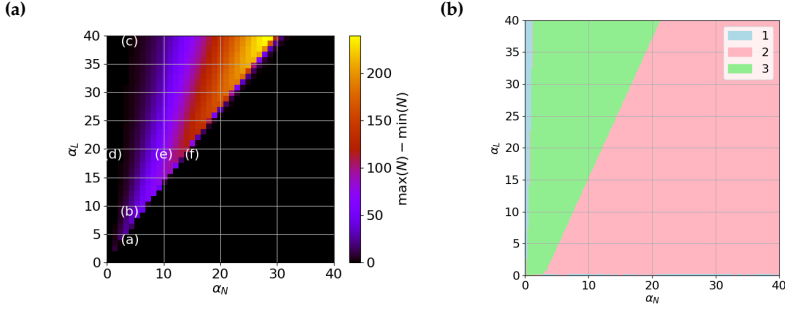


**Figure 5.5:** Using the parameter set *Adjusted*, patterns are formed when choosing the max. production rates  $\alpha_N$  and  $\alpha_L$  in the correct ranges. **5.5a:** Phase diagram of max. production rates of Nodal and Lefty  $\alpha_N$  and  $\alpha_L$ . For each combination of production rates, the difference between the global maximum and minimum Nodal concentration of 1d simulations at  $t^* = 100$  is shown by color. **5.5b:** Numerical approximation of the bifurcation diagram for the parameter set *Adjusted*, as derived in chapter 3.

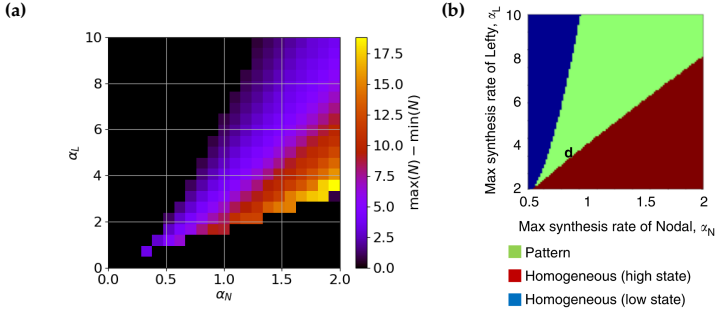


**Figure 5.6:** **5.6a:** Zoom-in on the bottom left corner of Figure 5.5a. **5.6b:** Phase diagram using the original parameter set, produced by Sekine et al. [9].

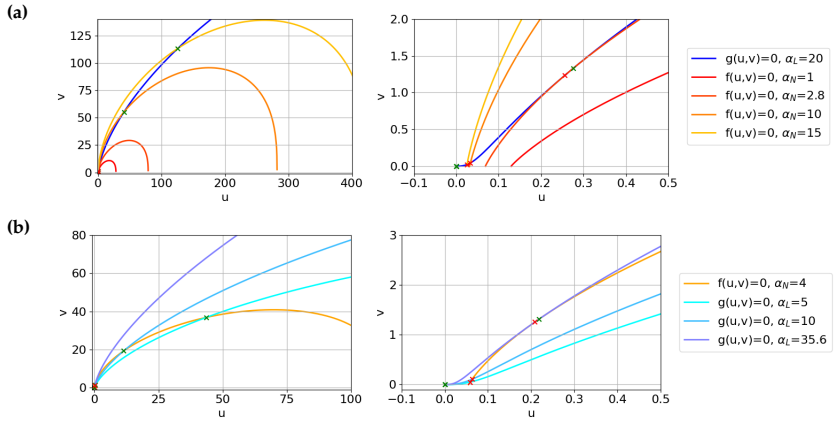


**Figure 5.7:** Nullclines  $f(u,v) = 0$  and  $g(u,v)$  for the dimensionless Nodal and Lefty equations respectively, using the parameter set *Adjusted*. Unstable and stable steady states were computed numerically and plotted as red and green crosses respectively. The right column presents a zoom-in view on the bottom left corner of the respective plots.



different regions of the phase diagram 5.5a. The labels (a) – (f) again match the ones from Figure 5.5a. The results are qualitatively similar to those in Figure 5.3. Simulations in the area below the bistable region (for lower  $\alpha_L$ ) lead to homogeneous high states (5.8a and 5.8f), whereas simulations from the area over the bistable region lead to homogeneous low states (5.8c and 5.8d). Within the bistable region, patterns are formed. Thereby, the interconnectivity of the pattern is higher the closer it is to the high state region. Closer to the low state region, we observe small circular regions of Nodal expression with low expression levels.

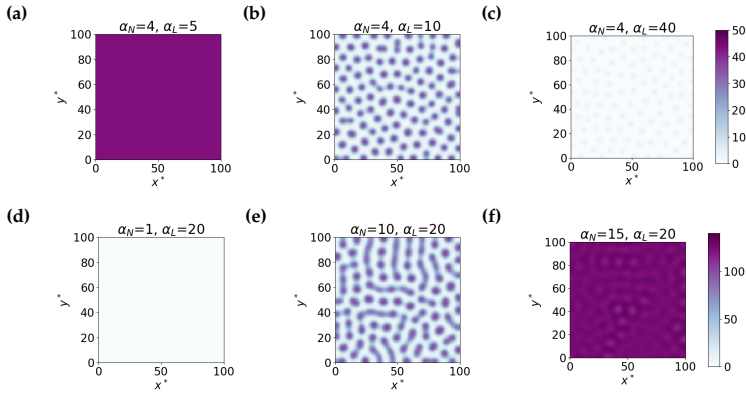


**Figure 5.8:** Pattern formations in Nodal concentration in 2-dimensinal simulations at  $t^* = 100$  for selected combinatinos of  $\alpha_N$  and  $\alpha_L$  using the parameter set *Adjusted*. The labels 5.8a - 5.8f correspond to the ones depicted in Figure 5.5a.

The experiment to determine the diffusion rate ratio  $d = \frac{D_L}{D_N}$  was carried out for the parameters *Adjusted* as well. The results are shown in Figure 5.9. The result differs slightly compared to *New*. We observe a critical value of  $d \approx 22$  over which pattern formation is possible. It seems however, that the parameter changes do not have a large influence on this value, as it still revolves around  $d = 20$ . The degradation-normalized diffusivity ratio  $\mathcal{R} = (\frac{D_L}{\gamma_L}) / (\frac{D_N}{\gamma_N})$  computes as  $\mathcal{R} \approx 9.23$ , which is in close proximity to the value  $\mathcal{R} \approx 8.3$  from *New* as well.

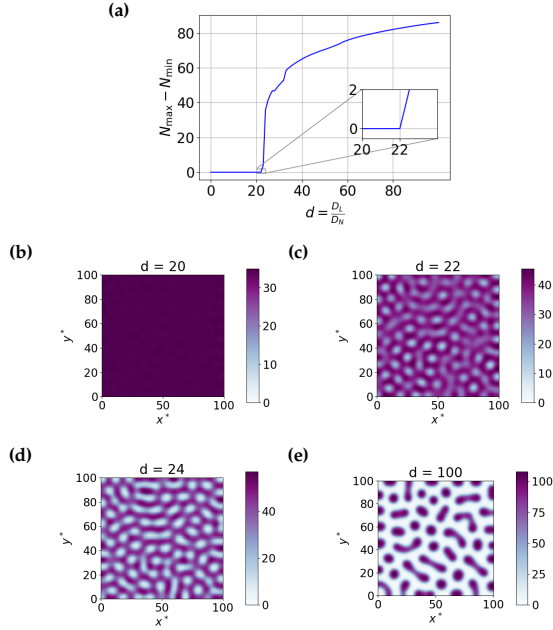


**Figure 5.9:** Dependence of pattern formation on diffusion rate ratio  $d = \frac{D_L}{D_N}$  using the parameter set *Adjusted* (see Tab. 5.1). **5.9b - 5.9e:** Pattern in Nodal concentration at  $t^* = 500$  for 2-dimensional simulations for 4 exemplary diffusion ratios  $d = 18, 20, 22, 100$ .

---

Through the exploration of the Nodal-Lefty model in this chapter we have gained an understanding of the general behavior of the model and how specific parameters influence the model's capacity to generate patterns. First, we found that achieving pattern formation required a suitable choice of the production rates  $\alpha_N$  and  $\alpha_L$ . The  $\alpha_N$ - $\alpha_L$  parameter space showed a clear region of pattern formation, the bistable region, which was shown to be in clear correspondence with the analysis of the nullclines. Therefore, we can be confident that the results of our simulation are consistent with mathematical predictions. Within the bistable region, the production rates determine which type of pattern is formed, producing patterns of varying interconnectivity.

We also observed that the ratio of diffusion coefficients ( $d = \frac{D_N}{D_L}$ ) is critical to pattern formation, with a clear threshold above which patterns are formed. This threshold varied slightly when choosing a different set of parameters, however it generally seemed to revolve around the value  $d \approx 20$ . These findings suggest that this is an inherent characteristic of the underlying model.

Moving forward, Chapter 6 will build on the findings regarding the diffusion rate ratio. We will investigate whether we can modify the model equations in order to get closer to a value of  $d = 1$ , i.e. similar diffusion rates for both Nodal and Lefty. This is motivated by an attempt to move the model closer to the physical properties observed for Nodal and Lefty.



## 6 Modifications to the Nodal-Lefty Model

It has been proposed, and we have confirmed also in the previous chapter, that patterning in reaction-diffusion systems requires higher diffusivity of the inhibitor in comparison to the activator [4][5]. Particularly, for our model we have found that the diffusion rate of Lefty needs to be at least 20 times higher than the one of Nodal. We know that Nodal-Lefty signaling is capable of patterning in real-world experiments from Sekine et al. [9]. However, it is unclear how the required difference in diffusivity comes to be. Interestingly, Nodal and Lefty are in fact of similar physical size, which would mean that in isolation, they should diffuse at similar rates. The difference in the effective diffusivity must therefore have a different origin.

The goal of this chapter is to modify our existing Nodal-Lefty model (3.1) in order to incorporate same diffusion rates for both Nodal and Lefty. For this effort, we add new terms and parameters to compensate for the changed diffusion rates in an attempt to find a model that is still capable of pattern formation.

### 6.1 Derivation of a Modified Model

Our approach is inspired by the idea that degradation rates can compensate for higher diffusion rates, which was explored in subsequent studies of Turing's work, e.g. by Gierer and Meinhardt [3]. This can be seen by a simple example of a diffusion model with linear degradation:

$$\frac{\partial y}{\partial t} = D \frac{\partial^2 y}{\partial x^2} - \gamma y. \quad (6.1)$$

The analytical steady state solution for this PDE can be computed as

$$y(x) = e^{-\lambda x} \quad \text{with } \lambda := \sqrt{\frac{\gamma}{D}}. \quad (6.2)$$

Evidently, one can achieve the same solution for different choices of  $\gamma$  and  $D$  as long as the ratio  $\frac{\gamma}{D}$  stays the same.

Consider a one-dimensional setting with a source term at position  $x = 0$ . We then consider the solution of (6.1) for a high diffusion rate  $D_{\text{high}} = 20\mu\text{m}^2/\text{s}$  with high degradation rate  $\gamma_{\text{low}} = 0.01/\text{s}$  and in another setting for a low diffusion rate  $D_{\text{low}} = 1\mu\text{m}^2/\text{s}$  with low degradation rate  $\gamma_{\text{high}} = 0.0005/\text{s}$ . For both cases we get  $\frac{\gamma}{D} = 0.0005$ . Figure 6.1 confirms that the analytical solutions in fact match exactly. If we compare this to our considerations from Figure 2.2a, this means that pattern formation is in theory possible with same diffusion rates and adjusted degradation rates.

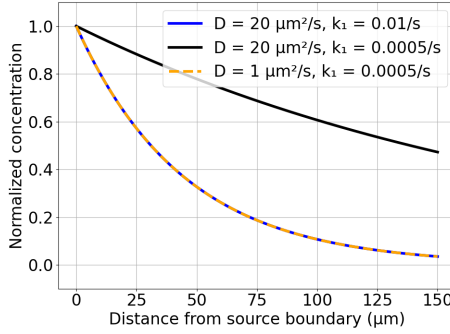


**Figure 6.1:** Analytical solutions of a diffusion-degradation model (6.1) for different diffusion and degradation rates. A high diffusion rate can be compensated by a high degradation rate in order to achieve the same profile.

We do not suggest that the effectively lower diffusion of Nodal is due to a higher degradation rate, or vice versa. This was also confirmed by Müller et al. [5]. However, our hypothesis is that the reason lies in different binding dynamics to cell receptors. If Nodal would have a significantly higher binding rate or lower dissociation rate, the result would be a lower effective diffusion.

Consider the following diffusion model with receptor binding, incorporated through a Michealis-Menten-type term:

$$\frac{\partial y}{\partial t} = d \frac{\partial^2 y}{\partial x^2} - \gamma \frac{y}{y + K} \quad (6.3)$$

Receptor binding can be seen as a nonlinear degradation term, which makes Equation 6.3 comparable to Equation 6.1. However, due to the nonlinear term, an analytical solution is not easily found. Thus, we opt for a numerical solution of (6.3) using finite differences. Again, we consider a source at  $x = 0$  and observe the concentration profile as the distance from the source increases. Similarly to Figure 6.1 we want to match the high diffusion profile to the low diffusion one. The matching is more difficult, because the effective degradation rate due to binding varies with concentration. At low concentrations  $y$  ( $y \ll K$ ) it behaves like linear degradation with rate  $\frac{\gamma}{K}$ . At high concentrations  $y$  ( $y \gg K$ ) it approaches a constant rate  $\gamma$ . In a first attempt, we try to match the profiles by simply scaling  $\gamma$  proportionally with  $D$ , as we did in the case of Figure 6.1. The result is shown in Figure 6.2. Although the scaling of the degradation rate  $\gamma$  was not exact, the profiles

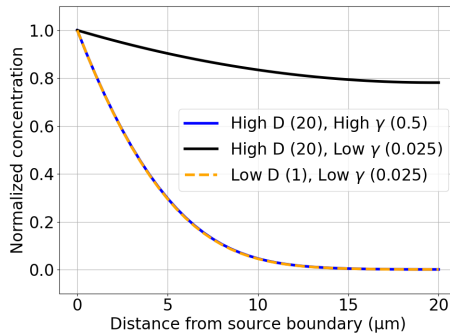


**Figure 6.2:** Finite difference approximations of a diffusion-binding model (6.3) for different diffusion and binding rates. A high diffusion rate can be compensated by a high binding rate in order to achieve the same profile.

still match well. The goal is now to incorporate such a binding term into the Nodal-Lefty model (3.1):

$$\frac{\partial N(x,t)}{\partial t} = F(N,L) + D \frac{\partial^2 N}{\partial x^2} \quad x \in \Omega, t \in [0,T] \quad (6.4a)$$

$$\frac{\partial L(x,t)}{\partial t} = G(N,L) + D \frac{\partial^2 L}{\partial x^2} \quad x \in \Omega, t \in [0,T] \quad (6.4b)$$

with the modified reaction terms

$$F(N,L) = \alpha_N \frac{N^{n_N}}{N^{n_N} + \left[ K_N^{\text{prod}} \left\{ 1 + \left( \frac{L}{K_L^{\text{prod}}} \right)^{n_L} \right\} \right]^{n_N}} - \gamma_N \frac{N}{N + K_N^{\text{bind}}} \quad (6.5a)$$

$$G(N,L) = \alpha_L \frac{N^{n_N}}{N^{n_N} + \left[ K_N^{\text{prod}} \left\{ 1 + \left( \frac{L}{K_L^{\text{prod}}} \right)^{n_L} \right\} \right]^{n_N}} - \gamma_L \frac{L}{L + K_L^{\text{bind}}}. \quad (6.5b)$$

The model (6.4) now has only one diffusion rate  $D$  for both Nodal and Lefty. The production in the reaction terms (6.5a) and (6.5b) remains the same, with the only exception being the renamed parameters  $K_N^{\text{prod}}$  and  $K_L^{\text{prod}}$ , to differentiate them from  $K_N^{\text{bind}}$  and  $K_L^{\text{bind}}$ . The linear degradation in (3.2) has been replaced by a term for receptor binding.

For the parameters we know from (3.1) we can use the same values as before, either from parameter set *Adjusted* or *New*. The new parameters are chosen such that the desired scaling proportional to the diffusion rates is achieved. Unfortunately, the modified model did not show pattern formation for this choice of parameters. Varying the parameters through trial and error also did not yield the desired result.

It remains uncertain whether this is inherent to the model or the right values for the parameters were simply not found. The python implementation of the derived model is openly available on [GitHub](#) for further research.

## 6.2 Explicit Receptor Binding

The model (6.4) derived in the previous section presents a simple approach to incorporate receptor binding into our Nodal-Lefty model. However, the Nodal-Lefty circuit as shown in Figure 2.4 describes the activation (or inhibition) of Nodal and Lefty as a result of Nodal (or Lefty) binding to cell receptors. This behavior is not described in (6.4). There, production and receptor binding are treated as separate processes.

In the following section we present a model which explicitly tracks the freely movable and receptor-bound concentrations of both Nodal and Lefty. This allows the connection of the production term to the receptor-binding process. The model (6.4) shows our proposed model. It involves incorporating reversible binding reactions between the signaling molecules (Nodal and



Lefty) and their respective receptors.

$$\frac{\partial N_f(x, t)}{\partial t} = \alpha_N \frac{N_b^{n_N}}{N_b^{n_N} + K_N^{n_N}} + d \frac{\partial^2 N_f}{\partial x^2} - \gamma_N N_f - k_{\text{on},N} R_N N_f + k_{\text{off},N} N_b \quad (6.6a)$$

$$\frac{\partial L_f(x, t)}{\partial t} = \alpha_L \frac{N_b^{n_N}}{N_b^{n_N} + K_N^{n_N}} + d \frac{\partial^2 L_f}{\partial x^2} - \gamma_L L_f - k_{\text{on},L} R_L L_f + k_{\text{off},L} L_b \quad (6.6b)$$

$$\frac{\partial N_b(x, t)}{\partial t} = k_{\text{on},N} R_N N_f - k_{\text{off},N} N_b \quad (6.6c)$$

$$\frac{\partial L_b(x, t)}{\partial t} = k_{\text{on},L} R_L L_f - k_{\text{off},L} L_b \quad (6.6d)$$

We introduce the variables  $N_f$  and  $L_f$  to denote the free concentrations of Nodal and Lefty, respectively, while  $N_b$  and  $L_b$  represent the concentrations of Nodal and Lefty bound to their receptors. The binding reactions are governed by association rates,  $k_{\text{on},N}$  and  $k_{\text{on},L}$ , and dissociation rates,  $k_{\text{off},N}$  and  $k_{\text{off},L}$ . The production terms for free Nodal and Lefty depend on the respective concentrations of bound Nodal and Lefty. The production is then modeled by a hill equation with hill coefficients  $n_N$  and  $n_L$  and the ligand concentrations producing half occupation  $K_N$  and  $K_L$ . Notice that the competitive inhibition is now modeled directly by tracking the bound Nodal and Lefty concentrations, not indirectly through the hill-type term like in Equation 3.1. Diffusion and degradation are only considered for the free species. The diffusion rate  $d$  is the same for both Nodal and Lefty. These modifications lead to a system of four coupled, non-linear, partial differential equations that describes the spatio-temporal evolution of free and bound forms of Nodal and Lefty and the interaction between the two signalling molecules and their respective receptors.

The newly derived model (6.6) involves even more unknown parameters than model (6.4). Moreover, the production term has been altered as well, which changes the parameters involved in the production. For these reasons, we were not able to observe pattern formation for this model as well.



## 7 Summary and Outlook

This thesis began by revisiting the Nodal-Lefty model proposed by Sekine et al. [9]. Through theoretical analysis of the governing equations we were able to make predictions, which we could later confirm in our numerical simulations.

Subsequently, we presented a detailed derivation of various discretization methods in order to find a numerical solution to the model equations. Thereby, we laid a special focus on versatility and adaptability, making it easy to modify or adapt the code for other reactions-diffusion systems.

First, we confirmed that the qualitative behavior of our simulations is in line with what we expect according to Murray [4]. We then identified a bistable region in the  $\alpha_N$ - $\alpha_L$  parameter space, which aligned with the theoretical predictions from the nullcline analysis. We also observed that the ratio of diffusion coefficients ( $d = \frac{D_N}{D_L}$ ) is critical to pattern formation, with a clear threshold above which patterns are formed. Our findings also align with previous studies on similar activator-inhibitor systems [5]. For those reasons, we can be confident in the validity of our implementation of the model.

We also explored the possibility of achieving pattern formation with equal diffusion rates for Nodal and Lefty by incorporating receptor binding kinetics into the model. Although we did not observe pattern formation using these modified models with the tested parameters, they provide a basis for future research aimed at making the model consistent with the physical properties of Nodal and Lefty. Moreover, these findings underscore the complexity of the Nodal-Lefty system and the difficulty of finding the right parameter ranges for pattern formation.

The results presented in this thesis suggest multiple opportunities for further research. Although concrete conditions on the production rates and the diffusion ratio have been found for specific parameter sets, we do not know how these depend on each other and on the other parameters. A more systematic exploration of the parameter space is needed to fully characterize the conditions under which patterns form.

The modified models incorporating receptor binding also require further investigation. It is possible that we simply did not find the correct parameter

regimes for pattern formation. However, there could also be an unknown factor inherent to the model which prevents it. A more systematic exploration of the parameter space or the inclusion of experimental data could help with answering these questions.

In conclusion, this thesis has contributed to our understanding of Turing pattern formation in the Nodal-Lefty signaling pathway. By developing a versatile simulation framework and exploring the model's behavior under different parameter regimes, we have provided a solid foundation for future research in this area. Ultimately, this work has not only demonstrated the complexity of Turing pattern formation within the Nodal-Lefty system, but has also raised new questions that inspire further research.

## Bibliography

- [1] Wikimedia Commons contributors. Giant pufferfish skin pattern detail, 2025. URL [https://en.wikipedia.org/wiki/Turing\\_pattern#/media/File:Giant\\_Pufferfish\\_skin\\_pattern\\_detail.jpg](https://en.wikipedia.org/wiki/Turing_pattern#/media/File:Giant_Pufferfish_skin_pattern_detail.jpg). Accessed: 2025-01-04.
- [2] Timothy S Gardner, Charles R Cantor, and James J Collins. Construction of a genetic toggle switch in *escherichia coli*. *Nature*, 403(6767):339–342, 2000. doi: 10.1038/35002131.
- [3] Alfred Gierer and Hans Meinhardt. A theory of biological pattern formation. *Kybernetik*, 12:30–39, 1972.
- [4] J.D. Murray. *Mathematical Biology II: Spatial Models and Biomedical Applications*. Springer, 3 edition, 2003.
- [5] Patrick Müller, Katherine W. Rogers, Ben M. Jordan, Joon S. Lee, Drew Robson, Sharad Ramanathan, and Alexander F. Schier. Differential diffusivity of nodal and lefty underlies a reaction-diffusion patterning system. *Science*, 336(6082):721–724, 2012. doi: 10.1126/science.1221920. URL <https://www.science.org/doi/abs/10.1126/science.1221920>.
- [6] Inc. Powers Scientific. Effects of lighting on zebrafish, 2025. URL <https://powersscientific.com/effects-of-lighting-on-zebrafish/>. Accessed: 2025-01-04.
- [7] ResearchGate. Modeling, analysis and simulation of nonperturbative nonlinear laser-gas interaction - scientific figure. [https://www.researchgate.net/figure/Symmetry-Strang-splitting-scheme\\_fig10\\_321198060](https://www.researchgate.net/figure/Symmetry-Strang-splitting-scheme_fig10_321198060), 2025. [accessed 6 Jan 2025].
- [8] Moritz Schweller. Master thesis repository. [https://github.com/schwelzmz/master\\_thesis](https://github.com/schwelzmz/master_thesis), 2025. Accessed: 2025-01-04.

- [9] Ryohei Sekine, Tatsuya Shibata, and Makoto Ebisuya. Synthetic mammalian pattern formation driven by differential diffusivity of nodal and lefty. *Nature Communications*, 9:5456, 2018. doi: 10.1038/s41467-018-07847-x. URL <https://doi.org/10.1038/s41467-018-07847-x>.
- [10] A. M. Turing. The chemical basis of morphogenesis. *Philosophical Transactions of the Royal Society of London. Series B, Biological Sciences*, 237(641):37–72, August 1952. doi: 10.1098/rstb.1952.0012. URL <http://links.jstor.org/sici?sici=0080-4622%2819520814%29237%3A641%3C37%3ATCBOM%3E2.0.CO%3B2-I>.

## Verwendung von KI-basierten Hilfsmitteln

Für einige Abschnitte der vorliegenden Arbeit wurden Textbausteine verwendet, welche mit Hilfe der Software ChatGPT 4o (openai.com) erzeugt wurden. Die Struktur und Aussagekraft einiger komplexerer Sätze wurde mit Hilfe von DeepL (deepl.com) verbessert.

## Eigenständigkeitserklärung

Ich versichere hiermit, dass ich, Moritz Schweller, die vorliegende Arbeit selbstständig angefertigt, keine anderen als die angegebenen Hilfsmittel benutzt und sowohl wörtliche, als auch sinngemäß entlehnte Stellen als solche kenntlich gemacht habe. Die Arbeit hat in gleicher oder ähnlicher Form noch keiner anderen Prüfungsbehörde vorgelegen. Weiterhin bestätige ich, dass das elektronische Exemplar mit den anderen Exemplaren übereinstimmt.

Weiterhin erkläre ich hiermit, dass ich beim Einsatz von IT-/KI-gestützten Schreibwerkzeugen diese Werkzeuge als verwendete Hilfsmittel mit ihrem Produktnamen, meiner Bezugsquelle und einer Übersicht des im Rahmen dieser Arbeit genutzten Funktionsumfangs vollständig aufgeführt habe. Bei der Erstellung dieser Arbeit habe ich durchgehend eigenständig und beim Einsatz IT-/KI-gestützter Schreibwerkzeuge steuernd gearbeitet.

8. Januar 2025

Ort, Datum



---

Unterschrift